DOES PRINTING DIRECTION INFLUENCE THE BOND BETWEEN 3D PRINTED POLYMERIC REINFORCEMENT AND CEMENTITIOUS MATRIX?

ROWIN J.M. BOL*, YADING XU*, MLADENA LUKOVIĆ† AND BRANKO ŠAVIJA*

* Delft University of Technology, Microlab, Faculty of Civil Engineering and Geosciences
Stevinweg 1, 2628 CN Delft, The Netherlands
e-mail: R.J.M.Bol@tudelft.nl, www.tudelft.nl

†Delft University of Technology, Concrete Structures Group, Faculty of Civil Engineering and Geosciences
Stevinweg 1, 2628 CN Delft, The Netherlands

Key words: 3D Printed Reinforcement, Additive Manufacturing, Bond Behaviour, Numerical Simulation, Lattice Beam Model

Abstract. The use of 3D printed polymers in the form of lattice reinforcement can enhance the mechanical properties of cementitious composites. Methods like Fused Deposition Modelling (FDM) 3D printing enable their creation, but this process has a large (negative) effect on their mechanical properties, with a large dependency on the printing direction. Continuing on our previous study concerned with modelling the anisotropic behaviour of 3D printed polymeric reinforcement, this work focuses on the reinforcement-matrix bond. Because of the layer-by-layer filament extrusion process of the 3D printing technique, the edges of FDM 3D printed polymers are typically composed of ellipses. Based on this, it is hypothesized that morphological effects as a result of the 3D printing technique enhance the bond between 3D printed reinforcement and cementitious matrix: The elliptic geometry potentially facilitates interlocking with the cementitious mortar, thereby possibly enhancing the bond behaviour in certain directions. To investigate the geometrical directional-dependent features at the edges of 3D printed polymers in more detail, micro-scale models are developed. Geometrical effects induced by different printing configurations are studied. The simulation results are verified through meso-scale pull-out experiments. The interlocking effects as a result of the 3D printing technique show to be significant seeing a bond strength increase of 56% compared to the direction without any geometrical effects.

1 INTRODUCTION

3D printed polymers in the form of lattice reinforcement can enhance the properties of cementitious composites [1–3]. However, the production process of such reinforcements has a large effect on their mechanical properties, with a large dependency on the direction of printing and loading [4]. Some concerns for 3D printed objects are, for instance, the containing of geometrical imperfections [5] and high level of anisotropy [6]. The layer-by-layer filament extrusion process of the 3D printing technique causes the edges of Fused Deposition Modelling (FDM) 3D printed polymers to be composed of ellipses [7]. The elliptic geometry potentially facilitates interlocking with the cementitious mortar, thereby possibly enhancing the bond behaviour in certain directions.

A methodology for determining the bond between cementitious matrix and 3D printed poly-

mers is explained, starting with pull-out experiments between FDM 3D printed Acrylonitrile Butadiene Styrene (ABS) bars and cementitious mortar (described in [8]), which are used to calibrate a meso-scale pull-out model. Morphological effects on the bond behaviour are studied by numerical simulations on two length scales using Lattice Beam Model (LBM) simulations. Bond properties are fist determined at the meso-scale using a pull-out model which resembles the pull-out experiments (as described in [8]). These pull-out tests are performed on ABS bars in which the printing path is parallel to the direction of loading to avoid any influence from the intra-layer and inter-layer bonds caused by the printing process [9]. Secondly, geometrical directional-dependent edge features of FDM 3D printed polymers are explicitly modelled at the micro-scale using the meso-scale properties as a reference. The material properties of the ABS bars for both the meso-scale and micro-scale models are adopted from our previous work [10] and are calibrated based on experimental results.

2 METHODOLOGY

2.1 Experimental analysis

The bond behaviour between FDM 3D printed ABS reinforcement and cementitious mortar will be determined from pull-out experiments described in our previous study [8]. The pull-out samples were created using 2×3 mm ABS bars with a length of 50 mm. The first 5 mm of the cementitious matrix was prevented to touch the ABS bar by means of a plastic tube with a radius of 5 mm and the embedded length was 10 mm. The dimensions of the pull-out specimens are depicted in Figure 1 and were loaded at a displacement rate of 5×10^{-3} mm/s.
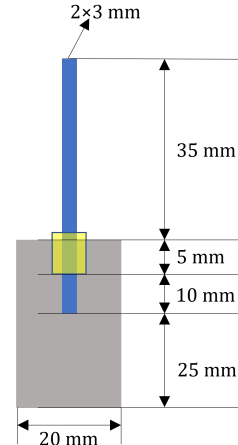
Figure 1: Dimensions of pull-out specimens [8]

Experimental pull-out results [8] are presented as bond stress-slip curves in Figure 2. The bond stress in Figure 2 is calculated using the actual circumference obtained from the expanded geometrical model described in [10], which describes the cross-sectional shape of 3D printed materials that are composed of ellipses having a larger contact area with the cementitious mortar. The geometric model has been implemented in the CAD application Rhinoceros® using Grasshopper to model the morphology of FDM 3D printed parts.
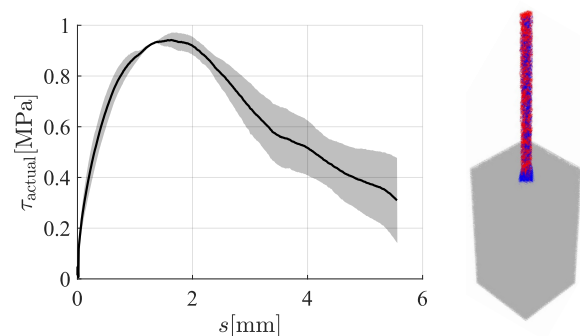
Figure 2: Experimental pull-out curves and numerical failure mode showing damage in blue

From the bond stress-slip results in Figure 2 it can be observed that the bond strength between FDM 3D printed ABS and cementitious matrix is very low, i.e. below 1 MPa. Because all experiments resulted in successful bar pull-out, the weak bonding can be attributed to the

fact that, at the molecular scale, ABS consists of hydrophobic groups [8]. As a result, there is no chemical adhesion with the cementitious mortar. Because of the absence of chemical adhesion, the bond strength mainly reflects the contribution of friction.

To better understand the bond behaviour between the FDM 3D printed ABS and cementitious matrix, Scanning Electron Microscope (SEM) pictures are taken to visualize the interface amongst the two materials. Figure 3 depicts two 20.0 kV images at different magnifications of 100 and 1000, clearly showing the elliptical morphology at the edges of the ABS 3D print. Furthermore, Figure 3 shows that the cementitious mortar has completely filled the sharp interior portions at the intersections between the stacked bead layers. This raised the hypothesis that interlocking effects as a result of the 3D printing technique could be facilitated, particularly in the inter-layer direction which has a strong resemblance with deformed reinforcement bars.
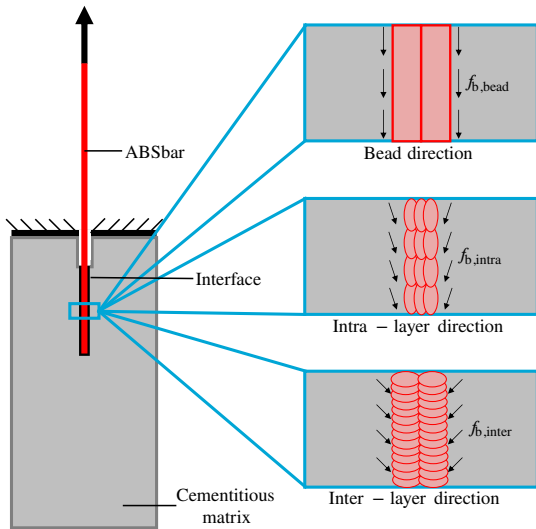
Figure 4: Bond behaviour of hypothesized mechanical interactions caused by different (local) shapes of reinforcements depending on printing path and build direction

Figure 4 illustrates the bond behaviour of the hypothesized mechanical interactions for the three different directions as a result of morphological effects. Please note that the intra-layer

and inter-layer directions are only investigated numerically at the micro-scale. These two directions can be regarded as if the ABS bars in the experiment were printed in the two mutually orthogonal build directions with respect to the bead direction.

2.2 Numerical simulations
2.2.1 Lattice beam model

In LBM simulations, a specimen is discretized into a network of lattice beam elements which enable load transfer [11–13]. As the ratio between length and cross-sectional size of the lattice beams is usually small, Timoshenko beam elements are applied to consider shear contributions [14–16]. The mesh can be made irregular and distinct input properties can be given to different elements [17], thereby including heterogeneity. The fracture process is captured via element removal, which may be lead by (step by step [11]) impairment of the element's stiffness [18].

The fracture process is initiated through the application of a certain load (i.e. deformation or force controlled), after which a linear elastic analysis is performed. During the analysis, stresses are recorded in all beam elements and assessed against the failure criterion in Equation (1):

$$\mathbb{F}(\sigma) = \frac{\sigma}{f_\mathrm{y}} \leq 1\,, \tag{1}$$

$$\sigma = \alpha_\mathrm{N}\frac{N}{A} + \alpha_\mathrm{M}\frac{\max\left(|M_i|, |M_j|\right)}{W}\,, \tag{2}$$

where σ is the stress computed using Equation (2) and f_y the material's strength. N is the normal force, A the cross-sectional area, M_i and M_j are the local bending moments in nodes i and j, W is the section modulus, α_N and α_M are the normal force and bending moment influence factors, respectively. Based on our previous study [10], α_N and α_M are taken as 1.0 and 0.05, respectively.

If one of the elements reaches the failure criterion in Equation (1), i.e. $\mathbb{F}(\sigma) = 1$, this element is removed from the latte network, thereby imposing damage. At this time, the load level
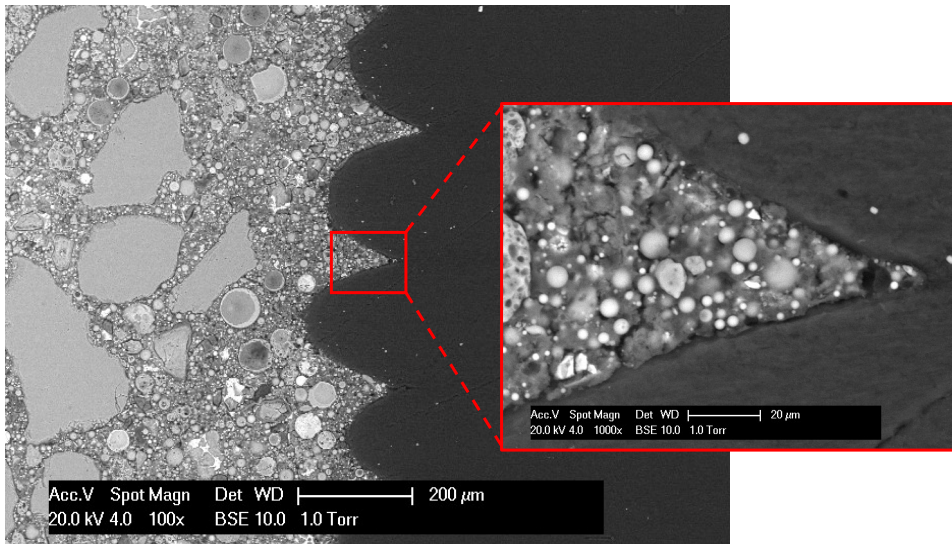
Figure 3: SEM picture of the interface between FDM 3D printed ABS and cementitious mortar

and displacement field are saved before reloading the updated (i.e. damaged) mesh and redoing the aforementioned procedure. The analyses continue through deleting elements exceeding the failure criterion one by one until the modelled specimen fails. The damage's intention is to replicate crack initiation and propagation. All linear-elastic analyses combined constitute a non-linear analysis containing detailed cracking information [11, 19].

The numerical procedure used here is similar to that of our previous work [10], but will be briefly explained next:

- The test specimen is discretized by a grid of cubic cells with length A as shown in Figure 5.

- Inside all cells, sub-cells having length s are created provided $0 \leq s \leq A$, see Figure 5. Every sub-cell contains one lattice node at a random location within its volume. Hence, $R = s/A$ defines the randomness of the lattice mesh, thereby including heterogeneity. In this work, R equals 0.5, except for lattice nodes at boundary conditions (i.e. load application and support locations). Boundary nodes have zero randomness to ensure even load distribution.

- Neighboring lattice nodes are connected by means of lattice beam elements along the three main axes (XX, YY, and ZZ), planar diagonals (XY, YZ, and XZ), and spatial diagonals (XYZ). To prevent intersecting diagonals, only the shortest are maintained.

- The phase of each lattice beam element is determined using two strategies, depending on the location of its two end nodes. The first strategy takes care that if both end nodes are located in the same region, the lattice beam element receives material properties belonging to that region (i.e. cementitious matrix in Figure 5). When the two end nodes are in different regions, such that the element crosses between them, it is considered an interfacial element having properties corresponding to that particular interface (i.e. ABS-matrix bond in Figure 5). The second strategy, proposed in [10], only concerns elements with both end nodes inside 3D printed material (i.e. ABS region in Figure 5). In that case, mechanical properties are assigned based on the element's orientation with respect to the printing path (n_i in Figure 5).

- Calibrations for each phase's stiffness

and strength are performed as described in [10] by means of an iterative determination procedure. For the constitutive relationships, multi-linear curves are used such that the elemental stiffness and strength are gradually altered during the analyses as illustrated in Figure 6.

Printing path-dependent lattice properties are assigned by introducing a local coordinate system consisting of unit vectors n_i, s_i and t_i. As shown in Figure 5, n_i corresponds to the ABS bar's longitudinal axis, which is parallel to the printing path, whilst s_i is perpendicular to n_i and lies in the same plane. t_i is the normal vector of this plane and is therefore not depicted in the two-dimensional representation in Figure 5. Directional element categories are imposed in every local coordinate system by means of spherical angles, where θ_{nst} is the azimuth angle of the projection on the plane formed by unit vectors n_i and t_i, measured from vector n_i, and ϕ_{nst} is the polar angle measured from the unit vector s_i. Now, the directional element categories can be decomposed into directional element domains in the local coordinate system with respect to the spherical angles. The decomposed directional element domains are listed in Table 1. Each colour of the lattice beam elements in Figure 5 corresponds to a different constitutive relationship. The input properties for the lattice beam elements corresponding to matrix phase are calibrated according to the experimental data presented in [20].
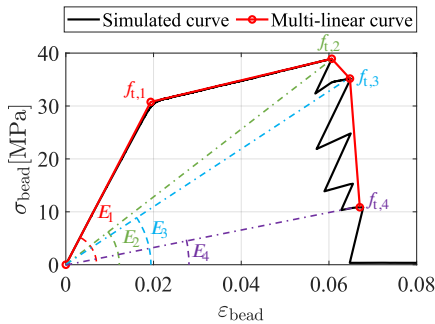
Figure 6: Multi-linear constitutive relationship for 3D printed ABS in uniaxial bead or **n** direction following Table 2 from our previous work [10]

2.2.2 Modelling procedure

The meso-scale model allows for calibration of the ABS-mortar bond properties through parameter fitting. The generated lattice mesh for the meso-scale pull-out simulations is displayed in Figure 5, having a mesh size of 0.6 mm. The input parameters for the ABS filament can therefore be taken from our previous study [10], which are provided in Table 2.

Once the ABS-mortar bond properties at the meso-scale are fitted with the experimental pull-out results, these are scaled down to the micro-scale. To enable explicit modelling of the microstructural morphology as a result of the FDM 3D printing technique (see [9]), a very fine mesh is required that would yield too computationally expensive numerical simulations at the meso-scale [8]. Therefore, taking into account the geometrical analyses described in [9] and Figure 3, three different directions with respect to the printing path will be studied by means of micro-scale LBM simulations: i) the bead or filament direction (parallel to the printing path, n_i), ii) the intra-layer direction (t_i), and iii) the inter-layer direction (s_i). Particularly the inter-layer direction has a strong resemblance with deformed reinforcement bars, see Figure 3.

The bead direction is the only direction that was successfully tested by means of pull-out experiments. It is therefore assumed that the bond behaviour between ABS and cementitious matrix is the same in terms of chemical adhesion and friction. Accordingly, morphological effects only contribute to the mechanical interaction through anchorage or interlocking of the mortar and elliptical edges.

2.2.3 Micro-scale models

At the micro-scale, a mesh size of 25 μm is used throughout all models. The out-of-plane model thickness is set to 750 μm with a matrix width kept constant at 1000 μm. All other dimensions related to the ABS bar correspond to the microstructural experimental analysis performed in [10] and are modelled via
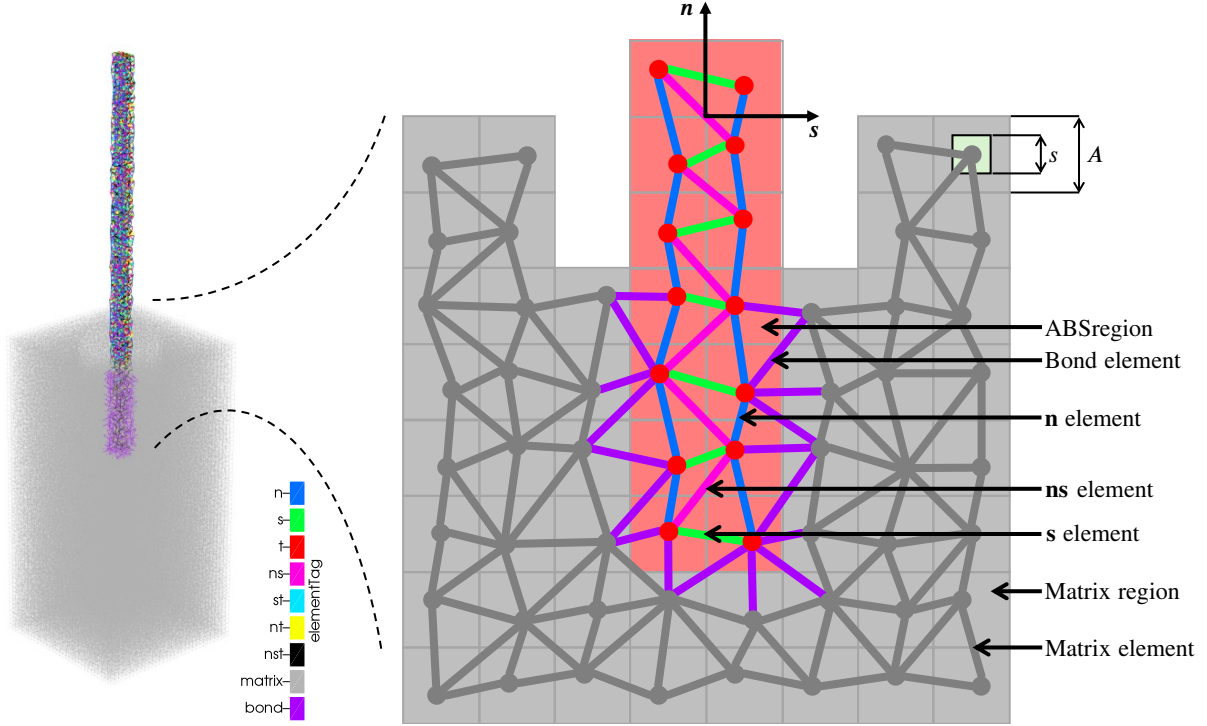
Figure 5: Generated lattice mesh for meso-scale pull-out model

Table 1: Directional element domains for property assignment from our previous work [10]

Directions	θ_{nst} (**rad**)	ϕ_{nst} (**rad**)
n	$\left[0, \frac{1}{8}\pi\right] \cup \left[\frac{7}{8}\pi, \frac{9}{8}\pi\right] \cup \left[\frac{15}{8}\pi, 2\pi\right)$	$\left[\frac{3}{8}\pi, \frac{5}{8}\pi\right]$
s	$[0, 2\pi)$	$\left[0, \frac{1}{8}\pi\right] \cup \left[\frac{7}{8}\pi, \pi\right]$
t	$\left[\frac{3}{8}\pi, \frac{5}{8}\pi\right] \cup \left[\frac{11}{8}\pi, \frac{13}{8}\pi\right]$	$\left[\frac{3}{8}\pi, \frac{5}{8}\pi\right]$
ns	$\left(0, \frac{1}{8}\pi\right) \cup \left(\frac{7}{8}\pi, \frac{9}{8}\pi\right) \cup \left(\frac{15}{8}\pi, 2\pi\right)$	$\left(\frac{1}{8}\pi, \frac{3}{8}\pi\right) \cup \left(\frac{5}{8}\pi, \frac{7}{8}\pi\right)$
st	$\left(\frac{3}{8}\pi, \frac{5}{8}\pi\right) \cup \left(\frac{11}{8}\pi, \frac{13}{8}\pi\right)$	$\left(\frac{1}{8}\pi, \frac{3}{8}\pi\right) \cup \left(\frac{5}{8}\pi, \frac{7}{8}\pi\right)$
nt	$\left(\frac{1}{8}\pi, \frac{3}{8}\pi\right) \cup \left(\frac{5}{8}\pi, \frac{7}{8}\pi\right) \cup \left(\frac{9}{8}\pi, \frac{11}{8}\pi\right) \cup \left(\frac{13}{8}\pi, \frac{15}{8}\pi\right)$	$\left(\frac{3}{8}\pi, \frac{5}{8}\pi\right)$
nst	$\left(\frac{1}{8}\pi, \frac{3}{8}\pi\right) \cup \left(\frac{5}{8}\pi, \frac{7}{8}\pi\right) \cup \left(\frac{9}{8}\pi, \frac{11}{8}\pi\right) \cup \left(\frac{13}{8}\pi, \frac{15}{8}\pi\right)$	$\left(\frac{1}{8}\pi, \frac{3}{8}\pi\right) \cup \left(\frac{5}{8}\pi, \frac{7}{8}\pi\right)$

Rhinoceros® using Grasshopper according to the geometrical models by Ahn et al. [7] and its extension in [21].

To see the isolated effect of morphological features without any influence of the intra-layer and inter-layer bonds within the 3D printed ABS material, another methodology to test micromechanical bond behaviour is used at the micro-scale, namely the push-out test [22]. By exposing the reinforcement to compression, tensile failure of the internal bonds will not be governing. Hence, given the same experimentally-fitted bond properties as before, push-out tests can measure the contribution of mechanical interactions.

To reduce computational costs only a half of each cutout is modelled in view of symmetry. To approximate experimental conditions, the loading and constraints are directly applied to the cutout portions of the ABS and surrounding matrix. However, note that the boundary conditions are modified to simulate push-out conditions. In total, four scenarios are modelled at the micro-scale: a reference for the intra-layer direction which mimics the bead direction (Figure 7(a)), the intra-layer direction containing two adjacent beads (Figure 7(b)), a reference for the inter-layer direction that reflects the bead direction (Figure 7(c)), and the inter-layer direction consisting of eight stacked layers (Figure

Table 2: Printing path-dependent directional element properties from our previous work [10]

Properties (MPa)	n	s	t	ns	st	nt	nst
E_1	1590	1570	1584	1912	1912	1923	2430
G_1	530	523.33	528	637.33	637.33	641	81
$f_{t,1}$	30.77	4.57	22.03	4.58	4.58	22.86	6.93
$f_{c,1}$	-38.46	-5.71	-27.54	-5.73	-5.73	-28.58	-8.66
E_2	642		980	812	789	775	1313
G_2	214		326.67	270.67	263	258.33	437.67
$f_{t,2}$	38.93		14.31	1.96	1.90	9.38	3.75
$f_{c,2}$	-48.66		-17.89	-2.45	-2.38	-11.73	-4.69
E_3	543			780	776	776	1256
G_3	181			260	258.67	258.67	418.67
$f_{t,3}$	35.18			15.39	10.74	15.26	22.06
$f_{c,3}$	-43.98			-19.24	-13.43	-19.08	-27.58
E_4	162			313	580	346	598
G_4	54			104.33	193.33	115.33	199.33
$f_{t,4}$	10.86			19.65	8.16	18.72	10.51
$f_{c,4}$	-13.58			-24.56	-10.20	-23.40	-13.14
E_5				275	90	295	514
G_5				91.67	30	98.33	171.33
$f_{t,5}$				17.49	1.28	18.43	15.28
$f_{c,5}$				-21.86	-1.60	-23.04	-19.10
E_6				82		89	211
G_6				27.33		29.67	70.33
$f_{t,6}$				5.34		6.12	19.44
$f_{c,6}$				-6.68		-7.65	-24.30
E_7							59
G_7							19.67
$f_{t,7}$							6.09
$f_{c,7}$							-7.61

7(d)). The two references in Figures 7(a) and 7(c) reflecting the bead direction are there to prevent any mesh dependencies when comparing the reference and morphological featured cases for the intra-layer and inter-layer, respectively. There is less polymer phase (i.e. ABS) in the micro-scale models for the intra-layer compared to the inter-layer (see Figure 7). Hence, due to the randomness of the lattice mesh and the difference in dimensions, a reference simulation for each direction is required to make a fair comparison.

3 RESULTS

3.1 Meso-scale constitutive relationship

The meso-scale bond stress-slip relationship is fitted with experimental pull-out data, similar to [8]. The starting point is to model the ABS bar, which is done in accordance with the printing path-dependent two-scale modelling scheme data explained in [10]. The local input for the matrix phase is calibrated with experimental data in [20] and lattice properties used in [8], corresponding globally to mortar with a Young's modulus of 11417 MPa. The local input therefore yields $E = 11417$ MPa, $G = 3805.7$ MPa, $f_t = 4.07$ MPa, and $f_c = -32.59$ MPa. Please note that local input (i.e. element properties) are always calibrated in such a way so that the global specimen response is achieved. Hence, depending on the mesh parameters (e.g. size and randomness), slightly different local properties are needed to mimic the same global behaviour [23].

The constitutive relationship for the bond elements between FDM 3D printed ABS bars and cementitious matrix is defined as a multi-linear curve composed of five segments (see Figure 8), similar to the pull-out models developed in [8]. Hence, their stiffness and strength are modified accordingly throughout the analyses rather than being directly discarded. The input parame-
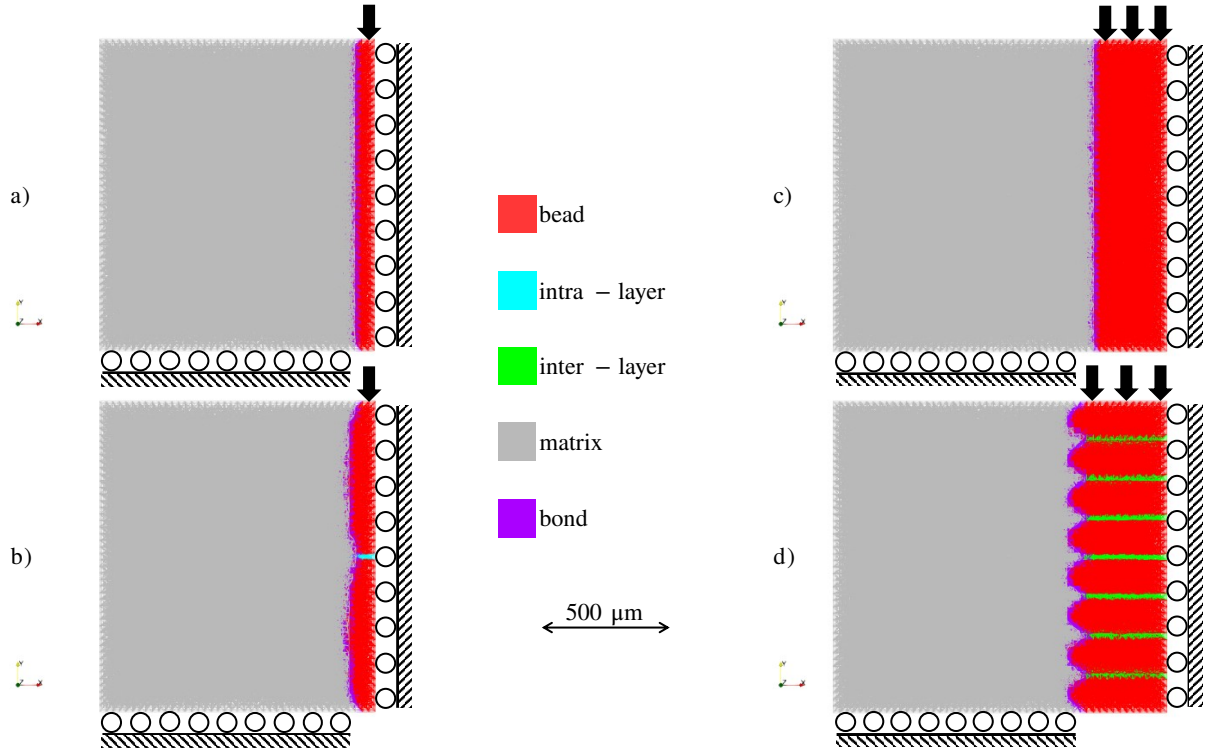
Figure 7: Generated lattice meshes for micro-scale push-out models of a) intra-layer reference, b) intra-layer direction, c) inter-layer reference, and d) inter-layer direction

ters for the bond phase regarding the meso-scale pull-out model in Figure 5 are contained in Table 3. The values for the ABS bars from [10], including the directional discretizations to capture their anisotropy, can be found in Table 2.
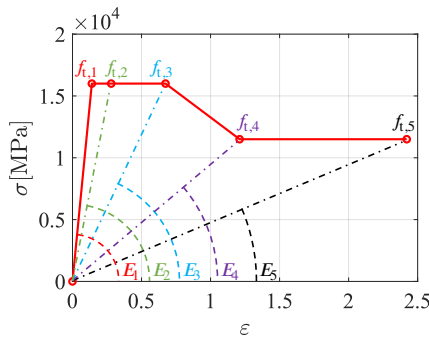
Figure 8: Multi-linear constitutive relationship for ABS-mortar bond

The shape of the multi-linear constitutive relationship for ABS-mortar bond in Figure 8 shows strong similarities with analytical models by Harajli et al. [24–26]. The implemented multi-linear constitutive relation approximates the experimental curves in a realistic manner as

shown in Figure 9. The maximum bond stress that can be reached without breaking the ABS bar in the LBM simulations is 0.8 MPa, which is about 16% lower compared to the experimental data.
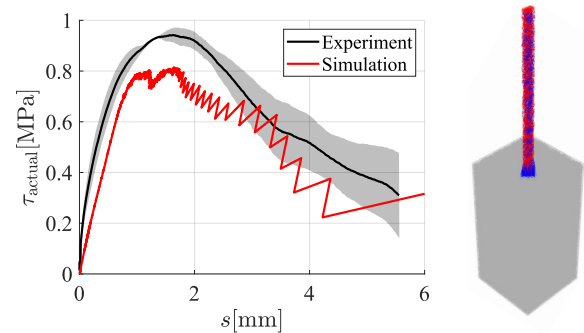
Figure 9: Comparison of meso-scale pull-out bond stress-slip curves and failure mode showing damage in blue

3.2 Micro-scale bond stress-slip analysis

Small virtual cutouts from the meso-scale pull-out experiments as described in Section 2.2.3 are subjected to LBM simulations of micro-scale push-out tests. The micro-scale

8

Table 3: Input for meso-scale ABS-mortar bond elements, following the curve shown in Figure 8

Properties	Segment 1	Segment 2	Segment 3	Segment 4	Segment 5
E_i (MPa)	114170	57085	23750	9500	4750
G_i (MPa)	38057	19028	7917	3167	1583
$f_{\mathrm{t},i}$ (MPa)	16000	16000	16000	11500	11500
$f_{\mathrm{c},i}$ (MPa)	-16000	-16000	-16000	-11500	-11500

bond stress-slip relationships resulting from the four scenarios described therein are displayed in Figure 10, maintaining the same format as Figure 7. However, the micro-scale slip values in Figure 10 cannot be compared to their meso-scale counterparts, because the latter include elastic deformation from the ABS bar whilst the former does not [27]. The micro-scale input for the bead, inter-layer and intra-layer phases is used from our previous work [10]. These are provided in Table 4, where the subscripts correspond to the segment number of a (multi-)linear curve (see Figure 6).

Table 4: Input parameters for micro-scale simulations

Properties (MPa)	Bead	Inter-layer	Intra-layer	Matrix
E_1	1590	1590	1590	11417
G_1	530	530	530	3805.7
$f_{\mathrm{t},1}$	40	6.6	29	4.23
$f_{\mathrm{c},1}$	-50	-8.25	-36.25	-33.84
E_2	343			
G_2	114.33			
$f_{\mathrm{t},2}$	38			
$f_{\mathrm{c},2}$	-47.5			

The local input for the matrix phase is recalibrated for the different mesh size at the micro-scale. Compared to the meso-scale simulations, in the micro-scale simulations the local strength input parameters for the matrix (see Table 4) and ABS-mortar bond elements (see Table 5) are slightly reduced.

Figure 10(a) shows the reference push-out behaviour for the intra-layer direction model which reflects the bead direction and therefore directly corresponds to the experimental pull-out observations. It can be seen that the obtained bond strength of about 0.73 MPa is almost identical to the meso-scale pull-out results in Figure 9 of about 0.8 MPa. This difference can be attributed to small differences in the lattice mesh because of its randomness.

Moreover, the shape of the pull-out bond stress-slip curve and failure mode are similar to those obtained experimentally and numerically at the meso-scale (see Figure 9). Please recall that the micro-scale slip values in Figure 10 are not comparable to the meso-scale as the latter include elastic deformation from the ABS bar whilst the former does not [27]. Furthermore, Figure 10(a) also includes the deformed mesh showing cracks in blue at final stage of the analysis which clearly indicates a clean push-out response. Figure 10(b) displays the intra-layer direction having a similar response with a slightly higher bond strength of nearly 0.84 MPa and also a clean pull-out with softening behaviour. Figure 10(c) depicts the reference pull-out behaviour for the inter-layer direction model which also corresponds to the bead direction. In this case, the obtained bond strength of 0.80 MPa perfectly matches the meso-scale pull-out results in Figure 9 and the fracture of the model also clearly indicates a clean push-out response. Figure 10(d) also displays a successful push-out in which the inter-layer bond within the ABS bar survives. Even though the peak is not as smooth as the others in Figure 10, a bond strength of about 1.24 MPa is reached. Therefore, this result truly shows the isolated effect of morphological features without any influence of the intra-layer and inter-layer bonds within the 3D printed ABS material. It can also be observed in Figure 10(d) that due to the wedging of the morphological features, some splitting of the matrix occurs.

The directional-dependent bond behaviour of the intra-layer and inter-layer directions at the micro-scale can be related to that of the bead direction using a strength ratio

$$r_{\mathrm{b},i} = \frac{f_{\mathrm{b},i}}{f_{\mathrm{b,bead}}}, \qquad (3)$$

9

Table 5: Input parameters for micro-scale ABS-mortar bond phase elements

Properties	Segment 1	Segment 2	Segment 3	Segment 4	Segment 5
E_i (MPa)	114170	57085	23750	9500	4750
G_i (MPa)	38057	19028	7917	3167	1583
$f_{t,i}$ (MPa)	12075	12075	12075	8682	8682
$f_{c,i}$ (MPa)	-12075	-12075	-12075	-8682	-8682

a) Intra − layer REF

c) Inter − layer REF

b) Intra − layer

d) Inter − layer
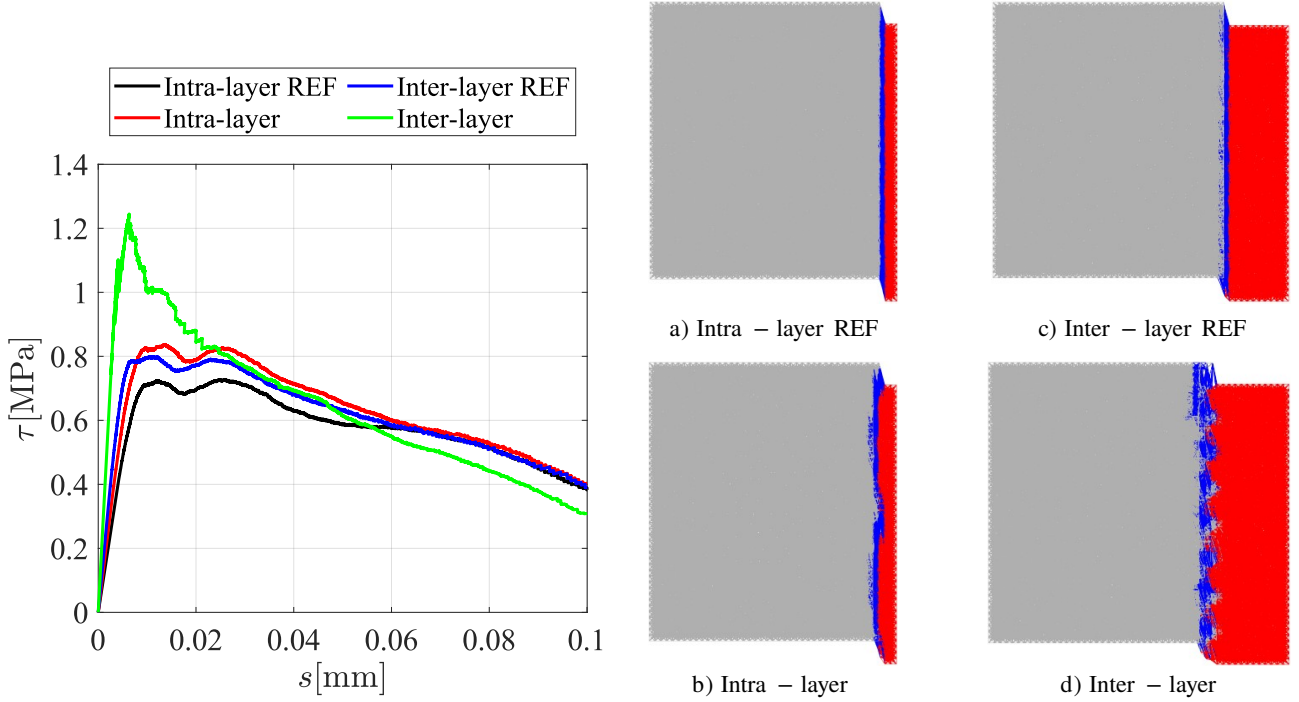
Figure 10: Micro-scale push-out simulation bond stress-slip and fracture results. Deformed meshes showing cracks in blue at final stage of the analyses.

where $f_{b,i}$ can be regarded as $f_{b,intra}$ and $f_{b,inter}$ corresponding to the bond strengths in the intra-layer and inter-layer directions at the micro-scale, respectively, and $f_{b,bead}$ is the bond strength in the bead direction at the micro-scale. Considering the directional-dependencies described by Equation (3), bond strength ratios of 1.15 and 1.56 are obtained for the intra-layer and inter-layer directions, respectively.

4 CONCLUSIONS

The presented work illustrates that printing direction influences the bond between 3D printed polymeric reinforcement and cementitious matrix. By explicitly modelling the geometry, and without changing input parameters, we learned what effect printing direction has on the bond between 3D printed polymeric reinforce-

ment and cementitious matrix. Interlocking effects as a result of the 3D printing technique in the inter-layer direction show to be significant, seeing a bond strength increase of 56% with respect to the (reference) bead direction (i.e. the 'bulk material' without interfaces perpendicular to the loading direction). However, these mechanical interaction effects in the intra-layer direction are found to be much smaller with a bond strength increase of only 15% compared to the reference direction. In conclusion, the hypothesized directional-dependent bond behaviour as a result of morphological features at the edges of FDM 3D printed ABS has been quantified and proven to exist.

REFERENCES

[1] Yading Xu, Hongzhi Zhang, Yidong Gan, and Branko Šavija. Cementitious composites reinforced with 3d printed functionally graded polymeric lattice structures: Experiments and modelling. *Additive Manufacturing*, 39, 3 2021.

[2] Shiwen Qin, Shuai Cao, Erol Yilmaz, and Jiajian Li. Influence of types and shapes of 3d printed polymeric lattice on ductility performance of cementitious backfill composites. *Construction and Building Materials*, 307, 11 2021.

[3] Can Tang, Junwei Liu, Wenfeng Hao, and Yuanyuan Wei. Flexural properties of 3d printed graded lattice reinforced cementitious composites using digital image correlation. *Materials and Design*, 227, 3 2023.

[4] Yading Xu, Hongzhi Zhang, Branko Šavija, Stefan Chaves Figueiredo, and Erik Schlangen. Deformation and fracture of 3d printed disordered lattice materials: Experiments and modeling. *Materials and Design*, 162:143–153, 1 2019.

[5] H. M.A. Kolken, K. Lietaert, T. van der Sloten, B. Pouran, A. Meynen, G. Van Loock, H. Weinans, L. Scheys, and A. A. Zadpoor. Mechanical performance of auxetic meta-biomaterials. *Journal of the Mechanical Behavior of Biomedical Materials*, 104, 4 2020.

[6] Athul Joseph, Vinyas Mahesh, and Dineshkumar Harursampath. On the application of additive manufacturing methods for auxetic structures: a review. *Advances in Manufacturing*, 9:342–368, 9 2021.

[7] Daekeon Ahn, Jin Hwe Kweon, Soonman Kwon, Jungil Song, and Seokhee Lee. Representation of surface roughness in fused deposition modeling. *Journal of Materials Processing Technology*, 209:5593–5600, 8 2009.

[8] Yading Xu, Zhi Wan, and Branko Šavija. Elevating mechanical performance of cementitious composites with surface-modified 3d-printed polymeric reinforcements. *Developments in the Built Environment*, 19, 10 2024.

[9] Rowin J. M. Bol and Branko Šavija. Micromechanical models for fdm 3d-printed polymers: A review. *Polymers*, 15:4497, 11 2023.

[10] Rowin J. M. Bol, Yading Xu, and Branko Šavija. Printing path-dependent two-scale models for 3d printed planar auxetics by material extrusion. *Additive Manufacturing*, 89, 6 2024.

[11] Mladena Luković, Hua Dong, Branko Šavija, Erik Schlangen, Guang Ye, and Klaas Van Breugel. Tailoring strain-hardening cementitious composite repair systems through numerical experimentation. *Cement and Concrete Composites*, 53:200–213, 2014.

[12] B. Šavija, G. E. Smith, D. Liu, E. Schlangen, and P. E.J. Flewitt. Modelling of deformation and fracture for a model quasi-brittle material with controlled porosity: Synthetic versus real microstructure. *Engineering Fracture Mechanics*, 205:399–417, 1 2019.

[13] Shozab Mustafa, Shantanu Singh, Dick Hordijk, Erik Schlangen, and Mladena Luković. Experimental and numerical investigation on the role of interface for crack-width control of hybrid shcc concrete beams. *Engineering Structures*, 251, 1 2022.

[14] Ze Chang, Hongzhi Zhang, Erik Schlangen, and Branko Šavija. Lattice fracture model for concrete fracture revisited: Calibration and validation. *Applied Sciences (Switzerland)*, 10, 7 2020.

[15] Nengdong Jiang, Hongzhi Zhang, Ze Chang, Erik Schlangen, Zhi Ge, and Branko Šavija. Discrete lattice fracture modelling of hydrated cement paste under uniaxial compression at micro-scale. *Construction and Building Materials*, 263, 12 2020.

[16] Ze Chang, Hongzhi Zhang, Minfei Liang, Erik Schlangen, and Branko Šavija. Numerical simulation of elastic buckling in 3d concrete printing using the lattice model with geometric nonlinearity. *Automation in Construction*, 142, 10 2022.

[17] Hongzhi Zhang, Yading Xu, Yidong Gan, Ze Chang, Erik Schlangen, and Branko Šavija. Combined experimental and numerical study of uniaxial compression failure of hardened cement paste at micrometre length scale. *Cement and Concrete Research*, 126, 12 2019.

[18] Nengdong Jiang, Zhi Ge, Yanhua Guan, Zhiwu Zuo, Hongzhi Zhang, Yifeng Ling, and Branko Šavija. Experimentally validated meso-scale fracture modelling of foamed concrete. *Theoretical and Applied Fracture Mechanics*, 122, 12 2022.

[19] Branko Šavija, Mladena Luković, José Pacheco, and Erik Schlangen. Cracking of the concrete cover due to reinforcement corrosion: A two-dimensional lattice model study. *Construction and Building Materials*, 44:626–638, 2013.

[20] Yading Xu and Branko Šavija. Auxetic cementitious composites (accs) with excellent compressive ductility: Experiments and modeling. *Materials Design*, 237:112572, 1 2024.

[21] L. Di Angelo, P. Di Stefano, and A. Marzola. Surface quality prediction in fdm additive manufacturing. *International Journal of Advanced Manufacturing Technology*, 93:3655–3662, 12 2017.

[22] Samanta Robuschi, Jakob Sumearll, Ignasi Fernandez, and Karin Lundgren. Bond of naturally corroded, plain reinforcing bars in concrete. *Structure and Infrastructure Engineering*, 17:792–808, 2021.

[23] A. Delaplace and R. Desmorat. Discrete 3d model as complimentary numerical testing for anisotropic damage. *International Journal of Fracture*, 148:115–128, 11 2007.

[24] M H Harajli, M Hout, and W Jalkh. Local bond stress-slip behavior of reinforcing bars embedded in plain and fiber concrete. *ACI Journal*, 92:343–353, 1 1995.

[25] Mohamed H. Harajli. Effect of confinement using steel, frc, or frp on the bond stress-slip response of steel bars under cyclic loading. *Materials and Structures/Materiaux et Constructions*, 39:621–634, 7 2006.

[26] M H Harajli. Bond stress-slip model for steel bars in unconfined or steel, frc, or frp confined concrete under cyclic loading. *Journal of Structural Engineering*, 135:509–518, 5 2009.

[27] Yidong Gan, Minfei Liang, Erik Schlangen, Klaas van Breugel, and Branko Šavija. Two scale models for fracture behaviours of cementitious materials subjected to static and cyclic loadings. *Construction and Building Materials*, 426:136107, 5 2024.